COMPUTATIONAL STUDY ON LEAD ALTERNATIVE PEROVSKITES FOR PEROVSKITE SOLAR CELLS

K.A.M.M.Kumarasinghe

188106T

Degree of Master of Science

Department of Materials Science and Engineering

University of Moratuwa,

Sri Lanka

June 2020

COMPUTATIONAL STUDY ON LEAD ALTERNATIVE PEROVSKITES FOR PEROVSKITE SOLAR CELLS

K.A.M.M.Kumarasinghe

188106T

Thesis submitted in partial fulfillment of the requirements for the degree

Master of Science

Department of Materials Science and Engineering

University of Moratuwa,

Sri Lanka

June 2020

DECLARATION

I declare that this is my own work and this thesis does not incorporate without acknowledgement any material previously submitted for a degree or diploma in any other University or institute of higher learning and to the best of my knowledge and belief it does not contain any material previously published or written by another person except where the acknowledgement is made in the text.

Also, I hereby grant to University of Moratuwa the non-exclusive right to reproduce and distribute my thesis/dissertation, in whole or in part in print, electronic or other medium. I retain the right to use this content in whole or part in future works (such as articles or books).

Signature: Date:

The above candidate has carried out research for the Master's thesis under my supervision.

Signature of the supervisor: Date

ABSTRACT

Hybrid organic-inorganic metal halide based perovskite solar cells (PSCs) lie at the heart of the emerging technologies of the solar cells due to their ability to increase the cell efficiencies dramatically over the last decade. $CH_3NH_3PbI_3$ based PSCs show the highest performances; still, the toxicity of Pb has been the limiting factor for the commercialization of organic lead iodide based solar cells. Thesis discusses about the variations of properties in terms of electronic and dielectric properties due to the substitution of Sn and Bi in place of Pb. A systematic study of ab-initio calculation on the electronic properties of $CH_3NH_3PbI_3$, $CH_3NH_3SnI_3$, and $CH_3NH_3BiI_3$ was performed. The results of the calculated band structures and the density of states of investigated materials reveal that $CH_3NH_3PbI_3$ exhibits an energy band gap, effective masses of charge carries, and available density of states in favorable values for high performance solar cells than those of $CH_3NH_3SnI_3$ and $CH_3NH_3BiI_3$. $CH_3NH_3PbI_3$ also consist of high dielectric capacity and better energy storage ability than $CH_3NH_3SnI_3$ and $CH_3NH_3BiI_3$. Above mentioned facts are the main reasons behind low-performance of Pb-free PSCs and it is paramount important to engineer the band gaps of those perovskites to obtain high performances.

Keywords: perovskite, efficiency, ab-initio, band gap, mobility, absorption coefficient

ACKNOWLEDGMENTS

I would like to start by thanking my research supervisor, Dr.(Mrs) A.S.Galhenage not only for her guidance throughout my research but also for the knowledge and experience that she has shared with me. I thank my supervisor for playing major role in my career development. Next, I would like to thank Dr.(Mrs) N.M.V.K.Liyanage from the University of Moratuwa and Dr. (Mrs.) M. L. C. Attygalle, senior lecturer from The University of Sri Jayawardenepura for their immense support and academic push throughout the evaluation procedure.

I would like to give my special thanks to the Center for Information Technology Services - University of Moratuwa (CITeS), Department of Mechanical Engineering and the Department of Computer Science and Engineering at University of Moratuwa for their the technical and computational support.

The staff [Academic and Non-academic] at the Department of Materials Science and Engineering, especially all the research assistants who were there with me working together is a main part of the success of this research. I would like to give my heartiest gratitude to all of them for being with me.

TABLE OF CONTENT

LIST OF FIGURES

LIST OF TABLES

CHAPTER1 INTRODUCTION

1.1 Introduction and Problem Statement

Organic-inorganic perovskite structured materials have become an emerging material for next generation of photovoltaic. The perovskite structure is introduced by the structure of mineral calcium titanate which has the chemical formula $CaTiO_3$.This perovskite structure is having the basic formula of ABX_3.With regard to hybrid organic-inorganic perovskite, A is an organic cation, B is an inorganic (metal) cation while X stands for the halide anion [1]. It is strongly believed that the perovskites would be the possible choice to substitute Si due to its outstanding structural, electrical and optical properties. Numerous researchers from various disciplines are going to be engaged in the intriguing field of perovskites to reveal more insight into the idea of the phenomenal properties of these materials in the next years.

The development of perovskite materials has altered the field of photovoltaic, after the first publication in 2009 [2]. The most significant member among the hybrid organic-inorganic PSCs is methyl ammonium lead iodide ($CH_3NH_3PbI_3$). Among the key optoelectronic properties of $MAPbI_3$ perovskite which makes it a dynamic material for photovoltaic, followings are highlighted [2]. Those are ideal band gap energy (about 1.55 eV), high absorption coefficient, reduced exciton binding energy, high charge-transporter mobility, great defect tolerance and long charge carrier diffusion lengths.

Furthermore, fabrication of $MAPbI_3$ is a low cost process due to the simple fabrication techniques and abundance of the raw materials. Among the significant restrictions for commercialization of $MAPbI_3$ based devices, high toxicity of Pb represents a hazard to people and causes natural defilement[3–5].

Researches have done numerous endeavors to substitute bivalent cation Pb^{2+} by Sn^{2+}, Sr^{2+}, Cd^{2+}, Ge^{2+}, Ca^{2+} and Bi^{3+}. Among the substitutions $CH_3NH_3GeI_3$ and $CH_3NH_3SrI_3$ are compatible in certain aspects, yet their high band gap brings about lower Power Conversion Efficiencies (PCEs) [6]. Substituting with Sn^{2+} observed a bandgap of 1.23eV which is really close to optimum bandgap of 1.34 eV. $CH_3NH_3SnI_3$ has the advantages of cost effectiveness and easy fabrication [7]. Bismuth, Bi^{3+} is an iso-electronic to Pb^{2+}, has an effective ionic

radius much close to Pb^{2+} [8]. The most attracting features of Bismuth are its non-toxic nature, stability at the room temperature, and easy synthesizing [8].

Among the above mentioned competitive substitutes, researchers have identified Sn and Bi as promising materials which need further studies to identify the possibility to replace Pb. Therefore, this study focuses on a comparative computational study on $CH_3NH_3PbI_3$, $CH_3NH_3SnI_3$ and $CH_3NH_3BiI_3$ to understand the effect of the substitution on the electronic properties, using energy band structures, density of states and frequency dependent dielectric function.

1.2 Objectives

Main objectives of the study can be highlighted as follows.

1. To investigate the doping techniques to tune the bandgap.
2. To study the band structures of the perovskite structured materials by computational modeling.
3. To identify the most suitable environmental friendly material with an optimum band gap energy.
4. To analyze the identified materials in terms of band structure, density of states and dielectric properties.

CHAPTER2 LITERATURE REVIEW

Researchers have carried out a complete and wide review of the past and current researches in this subject area. This chapter consists of the main results of previous research works to replace Pb perovskites and the required properties of a semiconductor material to be used in optoelectronic applications and different type of possible band gap engineering techniques.

2.1 Optoelectronic Properties

Optoelectronics are electronic devices that are used to detect or to control light. To be used in an optoelectronic device a material should possess certain properties such as appropriate bandgap, ferroelectric and dielectric behavior, defect tolerance, etc.

Band Structure and optical properties

Calculations of the band structure will reveal important information of optical and electronic properties of certain materials. Computational calculations based on Density Functional Theory (DFT) can be used to predict structures and dependable qualities of perovskites. Contributions from different atoms (A, B and X) to the optical properties can be explained by analyzing the band structure.

E.g.: The computations demonstrated that organic molecules are not legitimately associated with deciding the electronic structure of hybrid perovskites. According to Density of States (DOS) analysis of previous research works, commitment from the states of MA cations is immaterial around band edges of $MAPbI_3$. The organic molecule in halide perovskites basically works as a counter particle for settling the perovskite structure and charge balance.

Bandgap

Band gap is the most significant property of an optoelectronic material which decides the highest possible theoretical power conversion efficiency. The best solar absorbing effectiveness can be accomplished from the materials that have a bandgap in the scope of 1.1–1.56 eV, more favorably 1.3 eV [9]. This is an inherent property which will give the optionto comprehend whether the material can assimilate most of the solar energy (solar spectrum). How reasonable the materials are for photovoltaic applications would be controlled by how close the photon energy to the band gap of the material [10].

Defect tolerance

Imperfections or contaminations are identified as defects in a material. These defects affect the physical properties of the particular material. These imperfections can be seen in two different ways, for example, impurities and doping imperfections. They subsequently work as free transporters which empower charge recombination. As a result charge mobility is minimized [9]. Therefore various techniques are being utilized to control the defect tolerance of a certain material

Ferroelectric and dielectric behavior

Ferroelectric property gives a suitable path to isolate charge carriers immediately. In any case, the vast majority of the ferroelectric materials have wide-bandgap which is beyond the visible light spectrum range. This permits the utilization of solar energy to a minor rate (10–20%) [9]. The best advantage of the ferroelectric behavior is the high level of charge screening and restraining radiative electron–hole recombination. Ferroelectric property together with dielectric property (permeability) lead to littler defect binding energies advancing narrow deformity states [11].

2.2 Bandgap Engineering

Band gap engineering is a special process of altering the band gap of semiconducting materials to achieve any desirable optical or electronic transport properties. Some methods are briefly described below.

Dimensionality tailoring

Bandgap is engineered by changing the dimensionality of the material. 3D, 2D (sheets or plates), 1D (wires or bars), 0D (Quantum dabs) and also blended dimensional perovskite have been synthesized and tested. Improved overall performance has been examined with low dimensional structure [12]. Additionally, altering geometric size will also alter the bandgap.

Compositional substitution

Compositional designing is typically an extremely helpful and valuable strategy to adjust the band gap [13]. Halide (X) is the mostly effective position of the ABX_3 formula to enhance its properties by substitution. And also, substitution of the monovalent (A) and bivalent (B) results in band gap changing and broadened emission spectrum [12].

Phase segregation

This is related to the ion movement in the perovskites. Principle components to cause ion movements are light illumination and electric field. Light illumination and electric field have widely been reported as the causes for ion movement[12]. Separation of various phases which results in band gap alteration has been studied in mixed perovskites.

Phase transition

Thermal effect is a major reason for the phase transition. It can even reconstruct the structure results in a different space group of the material. However, thermal impact is not the only factor. Moisture also effects on phase change as a non-immaterial.

E.g.: Phase change from the $MAPbI_3$ tetragonal to cubic structure around 50 ^{0}C increasing the temperature.

Strain modulation

In this method, property changes were seen by changing the band gap by applying a tensile or compressive strain to the structure. In a much more extensive range of semiconductors, the strain has been broadly explored, and as needs are, strain engineering has been misused to alter the optoelectronic properties [14].

E.g.: The bandgap of 2D $MAPbI_3$ is getting wider during the tensile strain while compressive strain leads to narrow the band gap.

Pressure tuning

Applying a hydrostatic pressure to change the band gap has received the attention of recent researches. This technique doesn't involve chemical composition changing. Hydrostatic pressure causes changes in bond lengths and bond angles of the lattice structure which ultimately brings changes of the electronic band structure. Band gap narrowing or expanding, improvement of discharge power and prolongation of carrier lifetime and phase changes are some of the basic phenomena which are possible to occur due to pressure [15].

E.g.: $MAPbBr_3$ experiences a phase change alongside the band gap narrowing at mellow pressures of around 0.3GPa.

2.3 Lead Free perovskites

The elite of PSCs with moderately high strength, the existence of lead has received the attention of numerous scientists. Commercialization of this fabulous material has been discouraged due to the negative impact it causes on the environment and human. The main concern is the probability of releasing harmful compounds into the environment upon damaging the devices. Because of the above mentioned main issue of lead perovskite researchers are in an effort to supplant Pb while keeping its favourable properties and ultimately the market acceptance. Widely investigated and proposed materials so far are tin (Sn), bismuth (Bi), germanium (Ge) and copper (Cu).

Sn is a competitive substitution for Pb in perovskite solar cells because of its similarities in compound properties. The Sn-based perovskite has been utilized in transistors with surprising charge mobility [16]. Ogomi et al was one of the first to differ the organization of Pb: Sn proportion and attempted the demonstration of perovskite solar cells [17]. They had demonstrated the plausibility of Sn could be a potential choice as the absorber material for solar cells, yet in addition, indicated that unadulterated Sn perovskite solar cells didn't create any photovoltaic performance. It was likewise exhibited that Sn would ready to keep up its 2^+ oxidation state with the nearness of Pb in the absorption layer. Snaith et al. have manufactured an absolutely Pb free perovskite solar cells utilizing $MASnI_3$ as the perovskite light absorption with epitome and in nitrogen condition glovebox to forestall the debasement of the Sn-based perovskite absorber [18,19]. Notwithstanding the dependability issues, the study likewise referenced the plausibility of pb free perovskite to be utilized in perovskite solar cells with toxicity advantage over the Pb-based perovskite solar cells [20,21].

Sn based perovskite materials exhibit band gaps within the range from 1.1 to 1.7 eV [22]. Despite the negative fact that Sn^{2+} is easily oxidized to Sn^{4+}, higher electron and hole effective masses were positive parameters. When Pb and Sn are applied all the while ($MAPb_{1-x}Sn_xI_3$) in the absorber layer, it was discovered that the change in the bandgap does not corroborated with the degree of substitution. At the low concentration of Sn, the band gap diminishes, at that point least band gap at x = 0.5 and 0.75, subsequently the bandgap reached to 1.30Ev when Pb is completely substitute with Sn included [23,24].

Pb has been replaced by Ge together with Cs, Methyl ammonium and Formamidinum at the A position of ABX_3. Results revealed that these materials have somewhat higher bandgaps together with the issue of low stability. Their recorded effectiveness was just 0.2% [25].

Incorporating Cu into metal perovskite structure leads to specific results. 2D Cu based perovskite consists of a multi quantum-well electronic structure. It has introduced specific electronic and dielectric properties. Cu based perovskites experience very low power conversion efficiencies. Low absorption coefficient and higher hole effective masses are the identified causes for that.

Bi based perovskite has taken significant consideration because of its fascinating properties. Bi has introduced magnificent stability towards moisture and comparably less harmful in contrast to Pb. Past studies have exhibited the stability of $MA_3Bi_2I_9$ in surrounding conditions for over 40 days. Conventional and inverted planer structure has shown the effectiveness of just 0.19% and 0.1 [26]. Due to its sound properties together with less harmfulness, Bi based perovskite need more attention and more studies on it, to reveal its potential to be commercialized.

CHAPTER3 DENSITY FUNCTIONAL THEORY AND VASP

Vienna Ab-initio Simulation Package (VASP) is the software used here for the computational modeling. Density Functional Theory (DFT) is the theory of this computer simulation package. This chapter gives a clear and in depth description about DFT and VASP.

3.1 Density Functional Theory

Density functional theory is a method used to perform many-body quantum mechanical calculations computationally. This theory is applied to research or decide an electronic structure of a material which is difficult to be built up by experiments. Here we utilize functional to decide the properties of molecules or crystals. The standard function we consider here is the spatially reliant electron density. Thus we call it as Density Functional Theory.

In the majority of the cases DFT results concurs with the experimental results. Computational expenses for DFT calculations are low when contrasted with other customary techniques. This is the motivation behind why DFT is broadly utilized in recent time.

By and large, nucleus is large in size and mass and is thought to be steady (Born-Oppenheimer estimate) compared to the electrons in the atom. Then again electrons are light in weight and unpredictable to overlapping. Consequently electronic structure is considered as quantum mechanical issue. It is extremely perplexing in nature to comprehend.

3.1.1 Fundamentals of DFT

Any sort of quantum issue related to the matter or waves can be comprehended with the beginning of Schrodinger equation.

Schrodinger equation comes up with time-dependent and time-independent Schrodinger conditions. These equations are acceptable at anticipating the wave functions can bring about standing waves which are called as stationary states (additionally called "orbitals"). General time free Schrodinger condition can be composed as: [27]

$$E\psi = H\psi \qquad (1)$$

Where ψ is the wave function, E is the energy and H is the Hamiltonian operator.

Eq. 2 gives the Schrodinger equation of a single particle subjected to an electric field.

$$E\psi(r) = \left[\frac{(-\hbar)^2\nabla^2}{(2m)^2} + V(r)\right]\psi(r) \quad (2)$$

On account of electronic structure calculations of a many body system, Schrodinger equation can be written as eq. 3. In a many body system nuclei is treated as fixed amount which make static outer potential V. $\hat{T}$ denotes for the kinetic energy of the system. Coulomb interaction occurred due to the electron – electron repulsion is denoted by $\hat{U}$ [28].

$$H\psi = [\hat{T} + \hat{V} + \hat{U}]\psi = E\psi \quad (3)$$

3.1.2 Total energy from DFT

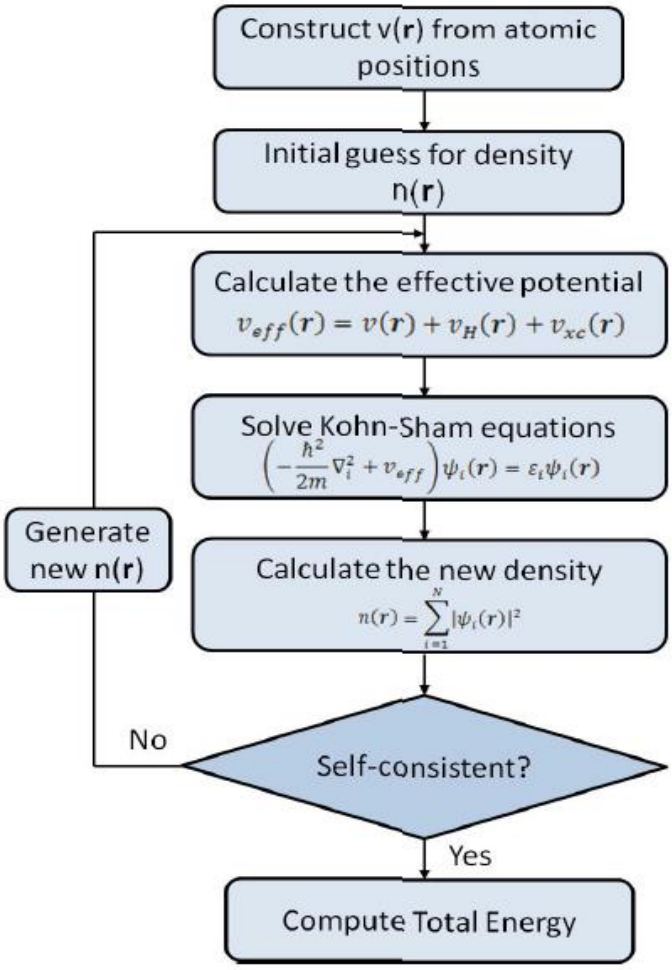

Figure 3. 1 Algorithm for calculation of total energy from DFT

Figure 3.1 represents the technique to acquire the all-out energy of framework utilizing DFT technique. At the initial step it develops the potential from the given nuclear positions. Later we have to make beginning supposition for electron density. At that point we should ascertain the effective possibilities utilizing this density function theory. In the accompanying advance

we can figure the Kohn-Sham equations utilizing powerful potentials, which can be utilized to compute new electron densities. This is the way we can acquire the all-out energy through arrangement of steps.

3.1.3 Exchange correlation approximations

There are some issues with DFT calculations, because of having foggiest idea about the accurate functions for exchange and correlation. To take care of this issue, there are any approximations which can be utilized in certain property computations. Most broadly utilized approximations are local-density approximation (LDA) and generalized gradient approximation (GGA).

3.1.3.1 Local density approximation (LDA)

As the vast majority of the properties of solids or frameworks rely upon absolute energy calculations, it is fundamental to get exact or exceptionally surmised estimations of total energy. According to the Hohenberg-Kohn hypothesis each parameter including exchange-energy is a component of electron density. So the easy method for portraying the exchange-correlation energy is to embrace local density approximation (LDA). Nowadays this guess is generally utilized for pseudo potential figuring.

Now the conditions related to the approximation are portrayed as underneath equation. Here, $\varepsilon_{XC}(r)$ is the exchange-correlation energy of electron at separation point r in the electron gas.

In LDA method $\varepsilon_{XC}(r)$ is assumed to be equivalent to the exchange-correlation energy per electron in homogenous electron gas.

$$E_{XC}^{LDA}[n(r)] = \int \varepsilon_{XC}(r) n\,(r) d^3r \tag{4}$$

And

$$\frac{\delta E_{XC}[n(r)]}{\delta n(r)} = \frac{\partial [n(r)\varepsilon_{XC}(r)]}{\partial n(r)} \tag{5}$$

Where

$$\varepsilon_{XC}(r) = \varepsilon_{XC}^{hom}[n(r)] \tag{6}$$

Here LDA estimate accepts that exchange-correlation energy is absolutely local. LDA counts the best suit for the energy of non-spin polarized framework, henceforth global energy least of vitality framework can be located by this plan. Anyway, there exists more than one least if there should arise an occurrence of magnetic materials. For this situation, so as to perform energy calculation the recreation expenses would be high.

3.1.3.2 Generalized gradient approximation (GGA)

The difference between LDA and GGA is that, GGA additionally takes the inclination factor of electron density at a similar area. We can say, without a doubt that it represents inhomogeneities when contrast with LDA approximations.

$$E_{XC}^{GGA}[\, n_{\uparrow}, n_{\downarrow}] = \int \varepsilon_{XC}(n_{\uparrow}, n_{\downarrow}, \nabla n_{\uparrow}, \nabla n_{\downarrow}) n(r) d^3 r \qquad (7)$$

There is another numerous functional for GGA approximations. Now r refers to the slope term of electron density which was not assumed in previous approximation [29].

Similarly, this utilitarian in other structure can be expressed as,

$$E_{XC}^{GGA}[n] = -C_x \int n^{\frac{4}{3}} F(s) dr \qquad (8)$$

Where

$$\mathrm{s} = \frac{\nabla_n}{2 k_F n} \qquad (9)$$

s is the proportion of inhomogeneity and k_F is the wave vector of homogenous electron gas with density n. So, these are scarcely any utilized approximations in DFT for the most part.

3.2 VASP

VASP represents Vienna Ab-initio Simulation Package. It is a mind-boggling bundle for performing reenactments for quantum-mechanical sub-atomic elements utilizing pseudo possibilities or the projector-enlarged wave technique and a plane wave premise set. VASP depends on the nearby thickness estimation. The variety amount is free vitality here, with the precise assessment of the immediate electronic ground state at each time step.

Ultra-delicate Vanderbilt pseudo possibilities (US-PP) and Projector-increased wave (PAW) portrays the cooperation among ions and electrons. They likewise take into account the significant decrease in the number of plane-waves per molecule for transition metals. With

the VASP we can figure the powers and stress tensors that can be utilized to loosen up the molecules into their ground states.

Answers for the many-body Schrodinger condition can be determined by VASP either by utilizing DFT or Hartree-Fock (HF) approximation. All in all, VASP utilizes a large number of input and output files.

3.2.1 Input files

Following are the four input files which are required in almost all VASP calculations.

3.2.1.1 INCAR File

INCAR file is responsible for all the commands to do required calculation and how to do it. There are lot of parameters related to different essential commands, most of which are by default. In general, a user who is unaware of all these parameters is not encouraged to change them because of its complexity.

For most of the calculations default set values are advisable to be used. Other than that, default values can be modified according to,

- The type of calculation required: Self/Non self-consistency calculation, Density of states, dielectric properties etc…
- The level of precision or the level of convergence required etc…

The mainly used tags for the calculations are described below. These are already set values and definitions by the developer of the VASP.

ISMEAR

"ISMEAR = -5 | -4 | -3 | -2 | -1 | 0 | [integer]>0

Default: ISMEAR = 1

ISMEAR determines how the partial occupancies are set for each orbital. SIGMA determines the width of the smearing in eV. ISMEAR = 0 was used in the calculations which stands for Gaussian Smearing"

EDIFF

"EDIFF = [real]

Default: EDIFF = 10-4

EDIFF specifies the global break condition for the electronic SC-loop.10-8 was used for the calculations"

ICHARG

"ICHARG = 0 | 1 | 2 | 4 | ≥10

Default: ICHARG = 2 if ISTART=0

= 0 else

ICHARG determines how VASP constructs the initial charge density.ICHARG = 11 was used for the 2nd step of the band structure calculation to obtain the eigenvalues (for band structure plots) or the DOS for a given charge density read from CHGCAR. If ICHARG≥10 the charge density remains constant during the run"

LORBIT

"LORBIT = 0 | 1 | 2 | 5 | 10 | 11 | 12

Default: LORBIT = None

LORBIT, together with an appropriate RWIGS, determines whether the PROCAR or PROOUT files are written".

Table 3. 1 Options of LORBIT tag

LORBIT	RWIGS tag	Files written
0	required	DOSCAR and PROCAR
1	required	DOSCAR and lm-decomposed PROCAR
2	required	DOSCAR and lm-decomposed PROCAR + phase factors
5	required	DOSCAR and PROOUT
10	ignored	DOSCAR and PROCAR
11	ignored	DOSCAR and lm-decomposed PROCAR
12	ignored	DOSCAR and lm-decomposed PROCAR + phase factors

IBRION

“IBRION = -1 | 0 | 1 | 2 | 3 | 5 | 6 | 7 | 8 | 44

Default: IBRION = -1 for NSW=−1 or 0

= 0 else

IBRION determines how the ions are updated and moved.

IBRION=-1: no update (ions are not moved)

IBRION=0: molecular dynamics is performed.

IBRION=1: ionic relaxation (RMM-DIIS).

IBRION=2: ionic relaxation (conjugate gradient algorithm).

IBRION=3: ionic relaxation (damped molecular dynamics).

IBRION=5 and 6: second derivatives, Hessian matrix and phonon frequencies (finite differences).

IBRION=7 and 8: second derivatives, Hessian matrix and phonon frequencies (perturbation theory).

IBRION=44: the Improved Dimer Method.”

ENCUT

“ENCUT = [real number]

Default: ENCUT = largest ENMAX value on the POTCAR file

ENCUT specifies the cutoff energy for the planewave basis set in eV”

PREC

“PREC = Low | Medium | High | Normal | Single | Accurate

Default: PREC = Medium for VASP.4.X

= Normal for VASP.5.X

PREC specifies the "precision"-mode. It is recommended to use PREC=Normal or PREC=Accurate. The settings PREC=Medium and PREC=High (available already in VASP.4.4) are no longer recommended. PREC=Normal can be used for most routine calculations, whereas PREC=Accurate reduces egg-box effects and errors even further"

ALGO

"ALGO = Normal | VeryFast | Fast | Conjugate | All | Damped | Subrot | Eigenval | Exact | None | Nothing | CHI | G0W0 | GW0 | GW | scGW0 | scGW | G0W0R | GW0R | GWR | scGW0R | scGWR | ACFDT | RPA | ACFDTR | RPAR | BSE | TDHF

Default: ALGO = Normal

The ALGO tag is a convenient option to specify the electronic minimization algorithm (as of VASP.4.5) and/or to select the type of GW calculations"

NBANDS

"NBANDS = [integer]

Default: NBANDS = NELECT/2+NIONS/2 non-spinpolarized

= 0.6*NELECT+NMAG spinpolarized

NBANDS determines the actual number of bands in the calculation"

LOPTICS

"LOPTICS = .TRUE. | .FALSE.

Default: LOPTICS = .FALSE.

This is the most important tag used in dielectric function calculation. "LOPTICS=.TRUE." calculates the frequency dependent dielectric matrix after the electronic ground state has been determined"

CSHIFT

"CSHIFT = [real]

Default: CSHIFT = OMEGAMAX*1.3 / max(NOMEGA,40) for GW calculations

= 0.1 for linear response calculations

CSHIFT sets the (small) complex shift η in the Kramers-Kronig transformation. The default CSHIFT=0.1 is perfectly acceptable for most calculations and causes a slight smoothening of the real part of the dielectric function"

NEDOS

"NEDOS = [integer]

Default: NEDOS = 301

NEDOS specifies number of grid points on which the DOS is evaluated. The energy range between EMIN and EMAX is divided into NEDOS intervals, the DOS for each corresponding energy, is written in DOSCAR"

3.2.1.2 POTCAR File

POTCAR file should contain the PAW datasets for every single atom sort determined in the POSCAR:

VASP accompanies a library of PAW datasets, (at least one) for most components of the periodic table. Important Data such as energy cutoffs, atomic mass, valency of atoms etc. are stated in POTCAR.

In a case where more than one atom is present in the system, you should link related PAW datasets in the same order as in POSCAR document. You ought not to mix PAW datasets produced with different exchange-correlation functionals.

The POTCAR file, as a rule, contains all the required pseudo potentials for each nuclear species which are utilized in the computation. We have to accurately build the POTCAR files if the quantity of species is multiple.

3.2.1.3 POSCAR File

POSCAR is a detailed document of the lattice geometry and the ionic positions of each atom.

3.2.1.4 KPOINTS File

The KPOINTS file contains all the K-point coordinates and weights or the necessary mesh size for making the K-point grid. Two configurations exist in ordinary.

- Entering all k-points explicitly
- K-points along high symmetry lines

3.2.2 Output files

VASP uses lot of output files. But let us discuss couple of important output files used in VASP.

3.2.2.1 OUTCAR

OUTCAR contains a detailed description of a VASP run, including all the input parameters, details of the individual electronic steps, stress tensors, forces subjected on the atoms, dielectric properties, etc.

The extent of the above mentioned output data which should be written onto OUTCAR file can be modified using the NWRITE-tag in the INCAR file.

3.2.2.2 OSZICAR & stdout

This file contains a summary of the self-consistency-run including free energies, SCF algorithm used for the calculation, energy convergence, etc.

3.2.2.3 CONTCAR & XDATCAR

CONTCAR file got the geometry data at the end of a run (after any geometric changes).

CONTCAR file can be directly used for a continuation run as the POSCAR file just by copying the CONTCAR data to POSCAR, because both CONTCAR and POSCAR have the same format.

XDATCAR file holds the updated ionic positions after each ionic step.

3.2.2.4 DOSCAR, CHGCAR & WAVECAR

CONTCAR file got the geometry data at the end of a run (after any geometric changes).

CONTCAR file can be directly used for a continuation run as the POSCAR file just by copying the CONTCAR data to POSCAR, because both CONTCAR and POSCAR have the same format.

XDATCAR file holds the updated ionic positions after each ionic step.

CHAPTER4 COMPUTATIONAL METHOD

All the calculations were done using the Vienna ab-inito simulation program (VASP) which is a complex computer program used to perform atomic scale materials modeling such as quantum-mechanical molecular dynamics and electronic structure calculations using first principles [1,21]. VASP is based on Density Functional Theory (DFT).

4.1 Band Structure Calculation

All computations and calculations were performed by VASP, with the generalized gradient approximation (GGA) as expressed by Perdew, Burke and Ernzerhof (PBE). All the potentials used in the calculations are PAW potentials. We used a plane-wave cutoff energy of 400 eV for the PBE calculations. The Brillouin zone was sampled using a 7×7×7 Monkhorst-Pack *k*-points mesh for all the investigated materials. The calculations without Spin Orbital Coupling have been used due to its insignificancy and property (too heavy) of Pb and I atoms [30].

Cell relaxations were done for all three investigated materials ($CH_3NH_3PbI_3$, $CH_3NH_3SnI_3$, and $CH_3NH_3BiI_3$) in order to calculate stable lattice parameters. These lattice constants were varied and fit into parabolic equation as a function of energy to obtain total minimum energy.

Resulted minimum energy cell parameters were used for band structure calculations. The self-consistent and non-self-consistent runs for desired K points had been done in band structure calculations.

4.2 Dielectric Properties Calculation

Step 1: Ground state calculation (Self-consistency run).

INCAR file

```
ISMEAR = 0      | Gaussian smearing
SIGMA = 0.01    | Set small smearing width
EDIFF = 1.E-8   | Set tight convergence criterium
```

Step 2: The Independent-Particle- Approximation

LOPTICS=.TRUE. tag should be included in the INCAR file.

INCAR file

ALGO = Exact	Exact diagonalisation of Hamiltonian
NBANDS = 64	Keep 64 bands after diagonalisation
LOPTICS = .TRUE.	Compute frequency dependent dielectric function in the IPA, using a sum over unoccupied states (perturbation theory)
CSHIFT = 0.100	Complex shift used in Kramers-Kronig transformation
NEDOS = 2000	Number of bins in the DOS histogram
ISMEAR = 0 SIGMA = 0.01	Gaussian smearing Set small smearing width
EDIFF = 1.E-8	Set tight convergence criterium

WAVECAR file consists of orbitals which is one of the output files of Step 1 is required for this calculation.

CHAPTER5 RESULTS AND DISCUSSION

5.1 Stability of Structures

The study of stability of crystal structure and predicting crystal packing are crucial for engineering. Therefore, the stability of $CH_3NH_3PbI_3$, $CH_3NH_3SnI_3$, and $CH_3NH_3BiI_3$ structures were investigated. Goldschmidt's tolerance factor (t) is an indication of the distortion and the stable phases of the crystal structure and it should be in the range of $0.8 < t < 1$, for the perovskite material to be more stable [21,30]. The mathematical expression for the tolerance factor is given by eq. (10) [31],

$$t = \frac{r_A + r_x}{\sqrt{2}(r_B + r_X)} \quad (10)$$

where, r_A, r_B and r_X are ionic radius of A, B and X of perovskite crystal formula ABX_3, respectively. The tolerance factors, calculated using equation [10], for $CH_3NH_3PbI_3$, $CH_3NH_3SnI_3$, and $CH_3NH_3BiI_3$ are 0.912, 0.922, and 0.956, respectively [32]. The high tolerance factor with more symmetry of crystal structure, results in a cubic structure, which would give a positive impact on the opto-electronic properties of perovskites [31]. Therefore, the structures of $CH_3NH_3SnI_3$ and $CH_3NH_3BiI_3$ should be ordered cubic structures and can expect comparable opto-electronic properties to $CH_3NH_3PbI_3$.

$CH_3NH_3PbI_3$ exists in three phases which are stable in different temperature ranges [10,33]. Body centered tetragonal phase is the most stable structure at room temperature; more precisely in between 160K and 330K. This phase is transformed in to cubic and orthorhombic phases above 330K and below 160K respectively[6,34].

The cell relaxation calculations (known as self-consistency run which is the 1st step of the ab-initio calculation process) were run to confirm the stability level of structure with changing the lattice parameter of the starting geometrical model for the tetragonal $CH_3NH_3PbI_3$, cubic $CH_3NH_3SnI_3$, and cubic $CH_3NH_3BiI_3$.

Total energies corresponding to different lattice parameters were plotted as a function of the cell volume. The cell volume of minimum free energy structure was taken as the most stable configuration of the system as shown in Figure 5.1.

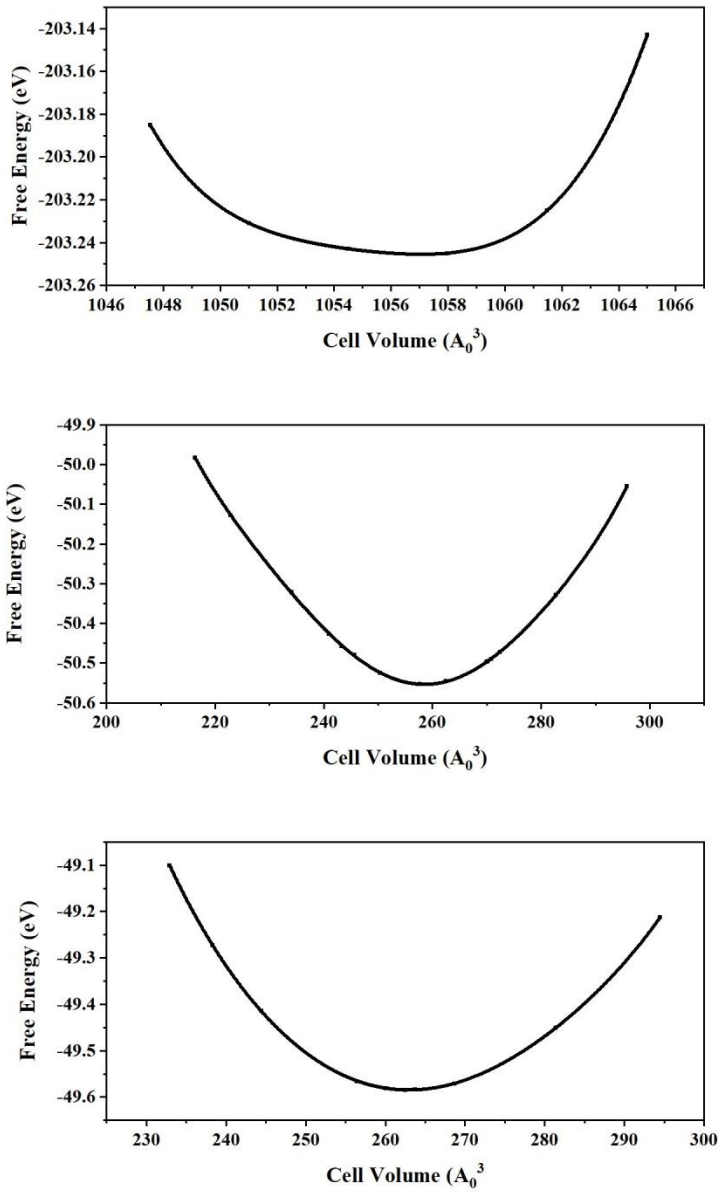

Figure 5. 1 Minimum cell energy curves for:

a) Tetragonal $CH_3NH_3PbI_3$; b) Cubic $CH_3NH_3SnI_3$, and; c) Cubic $CH_3NH_3BiI_3$

Resulted minimum cell energy parameters are listed in Table 5.1 and those minimum cell energy parameters were used to do further ab-initio calculations to obtain band structures.

Table 5. 1 Minimum cell energy parameters

Compound and Structure	Minimum Cell Energy Parameter	Literature Survey Data
Tetragonal $CH_3NH_3PbI_3$	a = b = 9.078	a = b = 8.856 [30]
Cubic $CH_3NH_3SnI_3$	a = 6.363	a = 6.243 [21] a = 6.248 [35]
Cubic $CH_3NH_3BiI_3$	a = 6.4029	-

5.2 Band Structure and Density of States Analysis

Band structure comprises of significant and must-know information, for example, the band gap, type of the band gap, effective masses of electrons and holes, densities of states and so forth which are essential for optoelectronic property observation.

This study critically analyzes the electronic band structures of $CH_3NH_3PbI_3$, $CH_3NH_3SnI_3$, and $CH_3NH_3BiI_3$. The calculated band structures for tetragonal $CH_3NH_3PbI_3$, cubic $CH_3NH_3SnI_3$, and cubic $CH_3NH_3BiI_3$ are given in Figure 5.2.

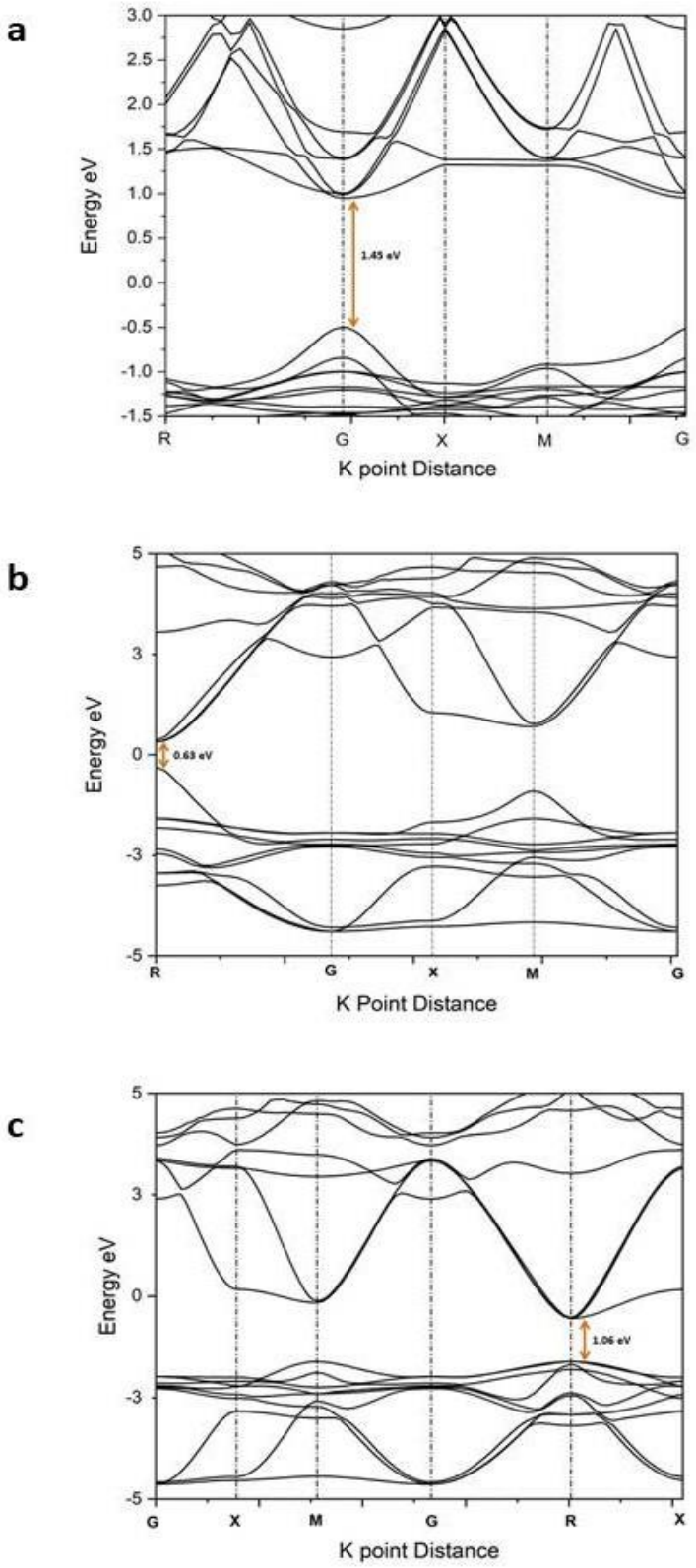

Figure 5. 2 Energy Band Structures for Tetragonal:

a) Tetragonal $CH_3NH_3PbI_3$; b) Cubic $CH_3NH_3SnI_3$, and; c) Cubic $CH_3NH_3BiI_3$

The band gaps were 1.45, 0.63 and 1.06 eV for tetragonal $CH_3NH_3PbI_3$, cubic $CH_3NH_3SnI_3$, and cubic $CH_3NH_3BiI_3$, respectively. All three investigated compounds show

direct band gaps. The band gap of the tetragonal $CH_3NH_3PbI_3$, positions on G symmetry point. Band gaps for the cubic $CH_3NH_3SnI_3$ and $CH_3NH_3BiI_3$ position on the M symmetry point and R symmetry point, respectively. Our calculated band gaps are comparative with previous research findings. A list of band gap values extracted from previous research findings can be seen in Table 5.2.

Table 5. 2 Comparison of resulted band gap values with previous research findings

Material	Resulted Band Gap [eV]	Previous research findings	
		Experimental [eV]	Theoritical [eV]
Tetragonal $CH_3NH_3PbI_3$	1.45	1.51 [36] 1.5 – 1.6 [37]	1.49 [37] 1.5 [38] 1.64 [39]
Cubic $CH_3NH_3SnI_3$	0.63	0.46 [8]	0.4 [40]
Cubic $CH_3NH_3BiI_3$	1.06	1.28 [36]	-

Electron transition is occurred by the photon in direct band gap materials. Solar cell which is a main optoelectronic device, supported direct band gap materials with higher optical absorption coefficients and band transition provided with photon energy[41].

Figures 5.3, 5.4, and 5.5 show an atom-projected electronic density of states (DOS) of $CH_3NH_3PbI_3$, $CH_3NH_3SnI_3$, and $CH_3NH_3BiI_3$ .Any way, these results do not include the effect of spin orbit coupling (SOC). Spin orbit coupling means the interaction of a particles' spin with its motion inside a potential.

.

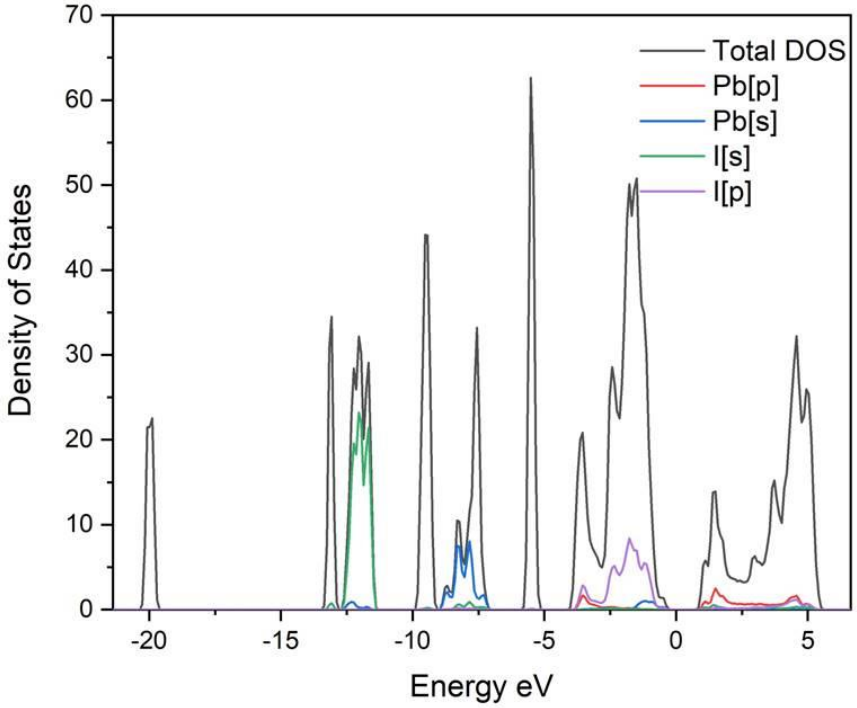

Figure 5. 3 Energy vs Density of States for $CH_3NH_3PbI_3$

As it is clearly seen in figure 5.3, I 5p states have dominated the valance band while Pb 6*s* and Pb 6p show less effect. Contribution of atomic orbitals are somewhat opposite in conduction band. Pb 6*p* contributes in a higher percentage while I 5*p* and 5*s* states show less contribution. The empty $CH_3NH_3^+$ ions are present above 5.6 eV and below -3.92 eV. So, the band gap is determined due to the overlap between Pb 6s/6p and I 5p states. The valance band of $CH_3NH_3PbI_3$ consists of four peaks while showing the highest peak of 50.795 at -1.49 eV. Among six peaks, the maximum peak of 32.235 at 4.57 eV was observed in the conduction band. Conduction band and valance band widths of $CH_3NH_3PbI_3$ were 4.86 eV and 3.92 eV.

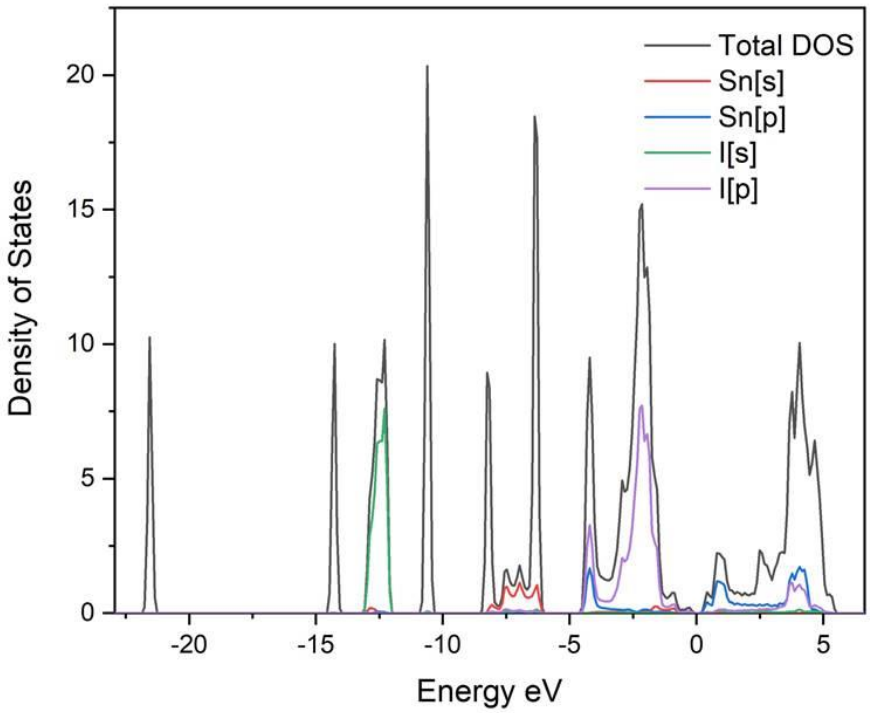

Figure 5. 4 Energy vs Density of States for $CH_3NH_3SnI_3$

As Figure 5.4 indicates, the percentage contributions of I 5p, Sn 6s, Sn 6p are similar to that of $CH_3NH_3SnI_3$ valance band. The empty $CH_3NH_3^+$ ions are present above 5.64 eV and below -4.61 eV. The Valance band of $CH_3NH_3SnI_3$ consists of six peaks while showing the highest peak of 15.211 at -2.15 eV. Among six peaks, the maximum peak of 10.046 at 4.06 eV was observed in the conduction band. The conduction band and the valance band widths of $CH_3NH_3SnI_3$ were 5.32 eV and 4.34 eV.

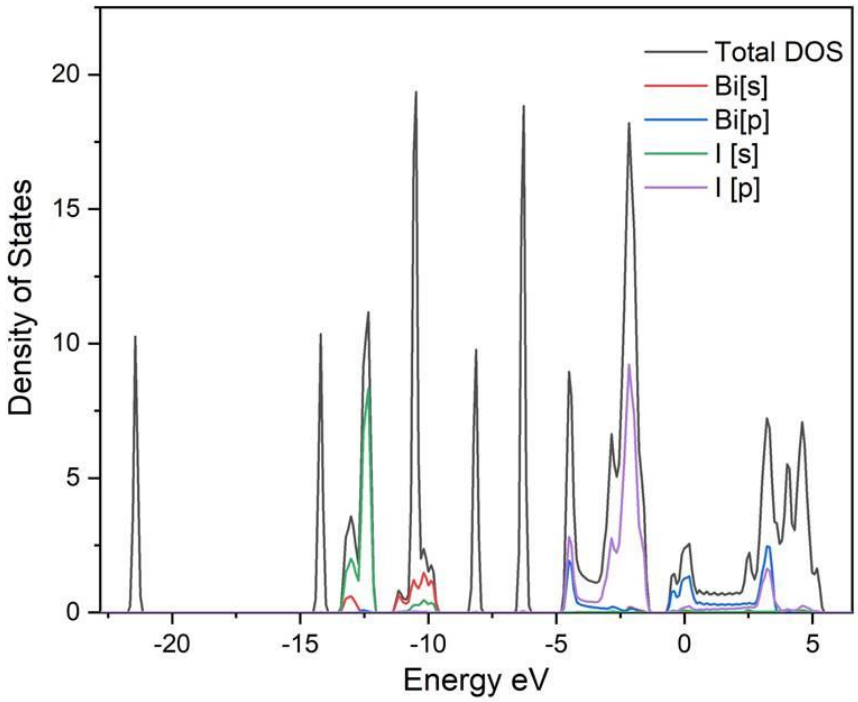

Figure 5. 5 Energy vs Density of States for $CH_3NH_3BiI_3$

Valance band maximum (VBM) of $CH_3NH_3BiI_3$ is also dominated by I 5p states. Similar as above two investigated materials, Figure 5.5 indicates that the valance band is mainly comprised of I 5*p* states with a small contribution of Bi 6*p* states while the conduction band is dominated by Bi 6*p* states with a less contribution from I 5*p* and 5*s* states for $CH_3NH_3BiI_3$ also. The empty $CH_3NH_3^+$ ions are present above 5.47 eV and below -4.80 eV. Therefore, the band gap of $CH_3NH_3BiI_3$ is determined by the overlap between Bi 6s/6p and I 5p states. Valance band of $CH_3NH_3BiI_3$ consists of three peaks while showing the highest peak of 18.2 at -2.16 eV. Among seven peaks, the maximum peak of 7.22 at 3.22 eV was observed in the conduction band. The Conduction band and the valance band widths of $CH_3NH_3BiI_3$ were 5.97 eV and 3.43 eV.

The contribution of different orbital states to valance bands and conduction bands of $CH_3NH_3SnI_3$ and $CH_3NH_3BiI_3$ shows some similarities to that of $CH_3NH_3PbI_3$. But, a difference in the extent of contributing at different critical energy levels (near valance band maximum point and conduction band minimum point) was observed. In the conduction bands, the contributions of Bi particles are less in the bottom of the conduction band while the impact of the Pb atoms rises towards the bottom of the conduction band.

Major component of VBM of $CH_3NH_3SnI_3$ is $CH_3NH_3^+$ similar to that of $CH_3NH_3PbI_3$. Contributions of Sn within the conduction band increase towards the bottom of conduction band which shows a similar behavior as $CH_3NH_3PbI_3$. Therefore, similar electrons behavior at critical energy levels of $CH_3NH_3PbI_3$ and $CH_3NH_3SnI_3$ can be observed while $CH_3NH_3BiI_3$ shows somewhat different electrons positioning.

At the point when the density of states diagrams of cubic $CH_3NH_3SnI_3$ and cubic $CH_3NH_3BiI_3$ were analyzed, it was seen that the commitments from the individual atoms of $CH_3NH_3SnI_3$ display a comparative behavior to the crystal structure of $CH_3NH_3PbI_3$ while $CH_3NH_3BiI_3$ shows a different atomic behavior.

Observed conduction band widths are 4.86 eV, 5.32 eV and 5.97 eV while the valance band widths are 3.92 eV, 4.34 eV and 3.43 eV for $CH_3NH_3PbI_3$, $CH_3NH_3SnI_3$ and $CH_3NH_3BiI_3$ respectively.

Identification of main differences among DOS graphs of $CH_3NH_3SnI_3$ and $CH_3NH_3BiI_3$ with respect to $CH_3NH_3PbI_3$, brought up key changes occurred in DOS graphs due to the metal cation substitution. The DOS graph of $CH_3NH_3SnI_3$ was compared with $CH_3NH_3PbI_3$. Conduction band and valance band widths of $CH_3NH_3PbI_3$ were 4.86 eV and 3.92 eV. But, conduction band and the valance band widths of $CH_3NH_3SnI_3$ were 5.32 eV and 4.34 eV. When it compares with $CH_3NH_3PbI_3$, the conduction band width has increased from 4.86 eV to 5.32 eV, while the valance band width has also increased from 3.92 eV to 4.34 eV. Therefore, replacing Pb with Sn has broadened both the conduction band width by 9.60 % and the valance band width by 10.56 %. However, substitution has significantly reduced the available DOS amount within the conduction and the valance bands. And it has reduced the total number of states within the conduction band from 535.54 to 142.09 while lowering the total states from 771.18 to 182.68 within the valance band due to the replacement of Pb by Sn.

Similarly, when it comes to $CH_3NH_3BiI_3$, conduction band width has increased to 5.97 eV while the valance band width has decreased to 3.43 eV. Therefore, replacing Pb with Bi has broadened the conduction band width by 22.97 % while narrowing down the valance band width by 12.65 %. And also, it is clear that the substitution has vastly reduced the available DOS amount within the conduction and the valance bands. It has reduced the total number of states within the conduction band from 535.54 to 143.06 while lowering the total states from 771.18 to 183.94 within the valance band due to the replacement of Pb by Bi.

The absorption coefficient (α) is another major factor which determines the successful electron excitation in to the conduction band. Semiconducting materials with higher

absorption coefficient more speedily absorb photons. For a direct semiconductor absorption coefficient straightly relies upon the accessible density of states and on the result of the densities of states of valence and conduction band for an indirect material [42,43].

We observed direct band gaps for all the investigated materials ($CH_3NH_3PbI_3$, $CH_3NH_3SnI_3$ and $CH_3NH_3BiI_3$). Total density of states for $CH_3NH_3PbI_3$, $CH_3NH_3SnI_3$ and $CH_3NH_3BiI_3$ are 1306.72, 324.77 and 327.00 respectively. Therefore, we can expect absorption coefficients in the order of $\alpha_{CH_3NH_3PbI_3} > \alpha_{CH_3NH_3BiI_3} > \alpha_{CH_3NH_3SnI_3}$.

5.3 Effective mass and charge carrier mobility

It is well known and well-studied that the charge carrier mobility of Methyl ammonium lead iodide has played a major role to make this material an outstanding candidate in the group of solar absorbing materials [44,45]. Masses of electrons and holes significantly affect charge carrier mobility and in this way on the productivity of the perovskite solar cell.

Effective mass can be obtained from the band structures using eq. (11) [46],

$$m^* = \frac{\hbar^2}{d^2E/dK^2} \tag{11}$$

In the above equation, m* denotes the effective mass; ħ stands for reduced plank constant and d^2E/dK^2 is the second derivative of energy with respect to k in the energy band structure. From the calculations, we got $0.01m_0$ and $0.03m_0$ as the effective mass of holes and the effective mass of electrons for $CH_3NH_3PbI_3$, respectively. And the effective masses of holes and electrons of $CH_3NH_3SnI_3$ are $0.08m_0$ and $0.02m_0$, respectively. Corresponding effective masses for $CH_3NH_3BiI_3$ are $0.15m_0$ and $0.02m_0$. All the resulted effective masses are listed in Table 7.3.

Table 5. 3 Calculated effective masses for investigated materials

Material	Effective mass of holes	Effective mass of electrons
$CH_3NH_3PbI_3$	$0.01m_0$	$0.03m_0$
$CH_3NH_3SnI_3$	$0.08m_0$	$0.02m_0$
$CH_3NH_3BiI_3$	$0.15m_0$	$0.02m_0$

It shows that both $CH_3NH_3SnI_3$ and $CH_3NH_3BiI_3$ have higher holes effective mass compared to $CH_3NH_3PbI_3$. But, both $CH_3NH_3SnI_3$ and $CH_3NH_3BiI_3$ have lower electron effective mass compared to $CH_3NH_3PbI_3$.

Key contention for low effective mass materials is its favorable impact on charge-carrier mobility. Charge Carrier mobility (μ) of a semiconductor can be calculated using the eq. (12) [47]

$$\mu = \frac{q\tau_m}{m_{eff}} \tag{12}$$

where μ, τ_m, q and m_{eff} are charge carrier mobility , momentum relaxation time, elementary charge and effective mass respectively. The mobility (μ) is corresponding to the proportion between the momentum relaxation time (τ_m) and the mass(i.e.$\mu \propto \tau_m/m_{eff}$) [43].

Three types of relations can be identified for lattice scattering, according to the type of phonons; namely polar optical phonons, acoustical phonons and first order phonons. For any type of lattice scattering, a lower effective mass results in higher carrier mobility [43].

Be that as it may, charge assortment essentially relies upon the mobility, lifetime, and all the more critically the thickness of the absorber layer. At last, the charge collection is a nonlinear capacity of the proportion of $\mu/d_{optimum}$ where $d_{optimum}$ is the ideal thickness of the solar engrossing layer which is characterized by the absorption coefficient [43]. Therefore, it is clear that the charge collection is encouraged by high charge mobility and lower optimum thickness. As the absorption coefficient straightly relies upon the accessible DOS, higher available DOS leads to a larger absorption coefficient. The higher absorption coefficient occurred due to the lower absorption depth subsequently lowering the optimum thickness.

From the results of the investigated materials, effective masses of $CH_3NH_3PbI_3$ ($0 < m^*_h < m^*_e < 0.05m_0$) are systematically lower than those of $CH_3NH_3SnI_3$ ($0 < m^*_e < m^*_h <$

$0.1m_0$) and $CH_3NH_3BiI_3$ ($0 < m^*_e < m^*_h < 0.2m_0$). Therefore, we can expect charge carrier mobility in the order of $\mu_{CH_3NH_3PbI_3} > \mu_{CH_3NH_3SnI_3} > \mu_{CH_3NH_3BiI_3}$.

As observed, available density of states of $CH_3NH_3PbI_3$ is significantly higher than both $CH_3NH_3SnI_3$ and $CH_3NH_3BiI_3$. The percentage of reduction of the available density of states in $CH_3NH_3SnI_3$ and $CH_3NH_3BiI_3$ is about 75 % with respect to that of $CH_3NH_3PbI_3$. As discussed in the previous section the higher density of states results in the higher absorption coefficient, subsequently a lower absorption layer thickness. We can expect $CH_3NH_3PbI_3$ to show a lower absorption layer thickness than $CH_3NH_3SnI_3$ and $CH_3NH_3BiI_3$. Therefore, in terms of optimum absorption layer thickness, $CH_3NH_3PbI_3$ is more favorable than $CH_3NH_3SnI_3$ and $CH_3NH_3BiI_3$.

5.4 Dielectric Function

Dielectric function refers to the permittivity of a material when the material is function of space and frequency. It is a complex value consists of a real and complex part where real part is connected to the polarization while the physical meaning of the complex part is the energy dissipation to the medium.

Having an idea of the dielectric loss of the material gives a clear view of the material's dissipation of energy. Loss tangent is the measurement of the dielectric loss.

5.4.1 Frequency dependant dielectric function

The dielectric behaviour is one of the most significant quantities that portrays the electrical and optical properties of solids.

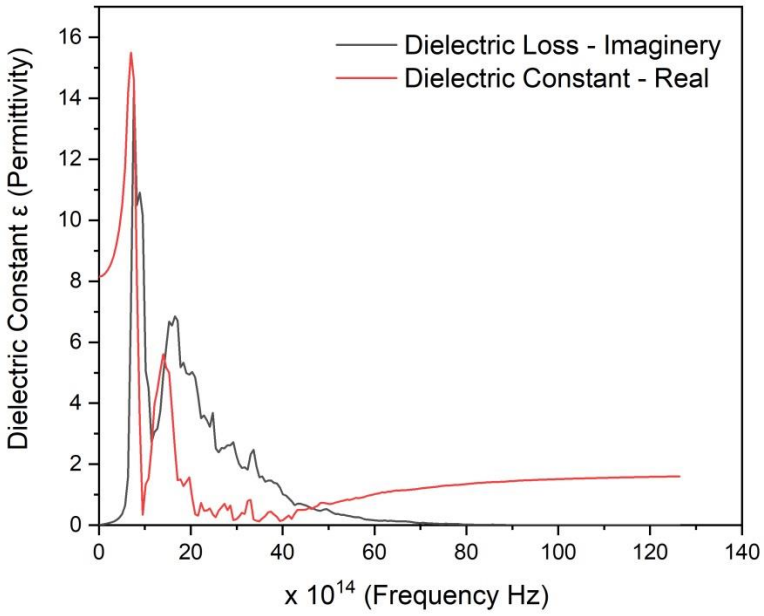

Figure 5. 6 Dielectric function of cubic $CH_3NH_3PbI_3$

Imaginary function – 2 peaks

Peak 1: 14.3824 at 7.6248 x 10^{14} Hz

Peak 2: 6.8517 at 16.5204 x 10^{14} Hz

Real function – 2 peaks

Peak 1: 15.5031 at 6.9894 x 10^{14} Hz

Peak 2: 5.6078 at 13.9788 x 10^{14} Hz

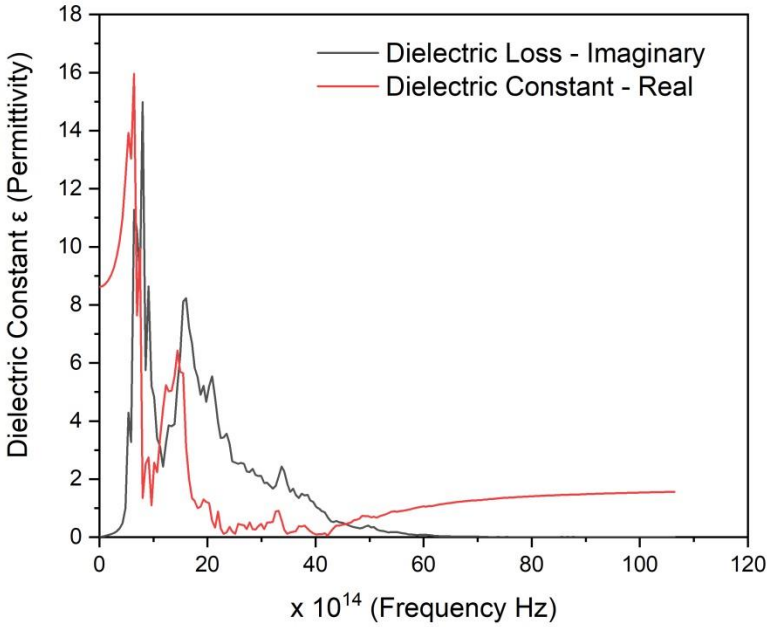

Figure 5. 7 Dielectric function of cubic $CH_3NH_3SnI_3$

Imaginary function – 2 peaks

Peak 1: 14.9823 at 8.0233 x 10^{14} Hz

Peak 2: 8.2382 at 16.0466 x 10^{14} Hz

Real function – 2 peaks

Peak 1: 15.9679 at 6.4186 x 10^{14} Hz

Peak 2: 6.4336 at 14.4420 x 10^{14} Hz

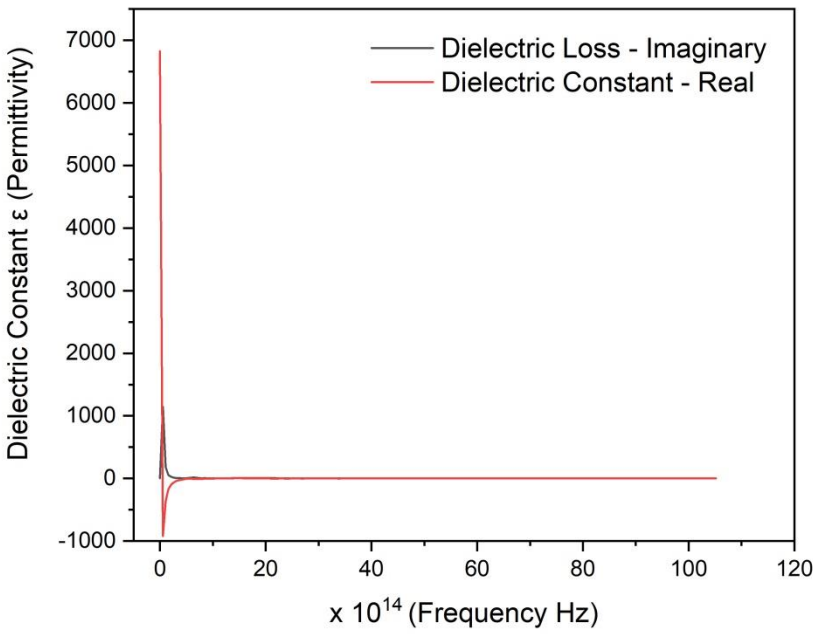

Figure 5. 8 Dielectric function of cubic $CH_3NH_3BiI_3$

Imaginary function – 1 peak

Peak 1: 1147.2479 at 0.5285 x 10^{14} Hz

Real function – 2 peaks

Peak 1: 6826.225 at 0 Hz

Peak 2: -920.033 at 0.5285 x 10^{14} Hz

5.4.2 Loss tangent

Loss tangent is a measure of energy saving capacity of the material. If the material shows a low loss tangent it leads to a "fast" substrate and wise versa.

Dielectric Function = $\varepsilon_{Imaginary} + \varepsilon_{Real}$

$$\textbf{Tan } \delta = \frac{Imaginery\ Part}{Real\ Part}$$

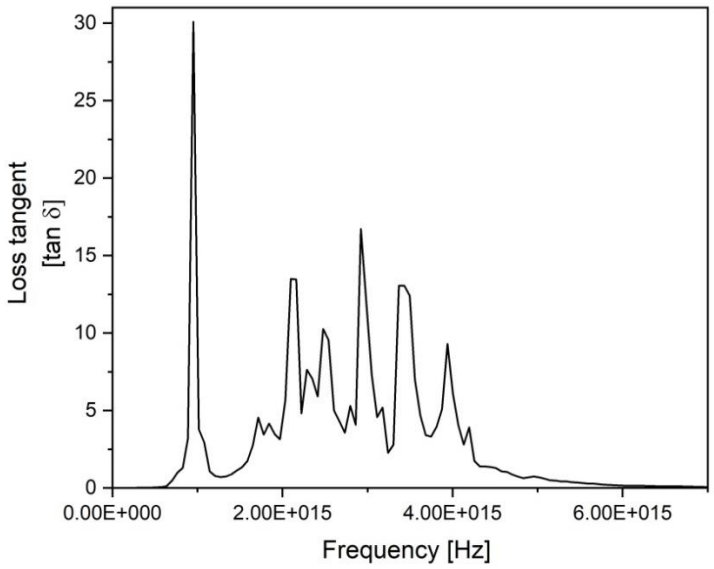

Figure 5. 9 Loss Tangent of cubic $CH_3NH_3PbI_3$

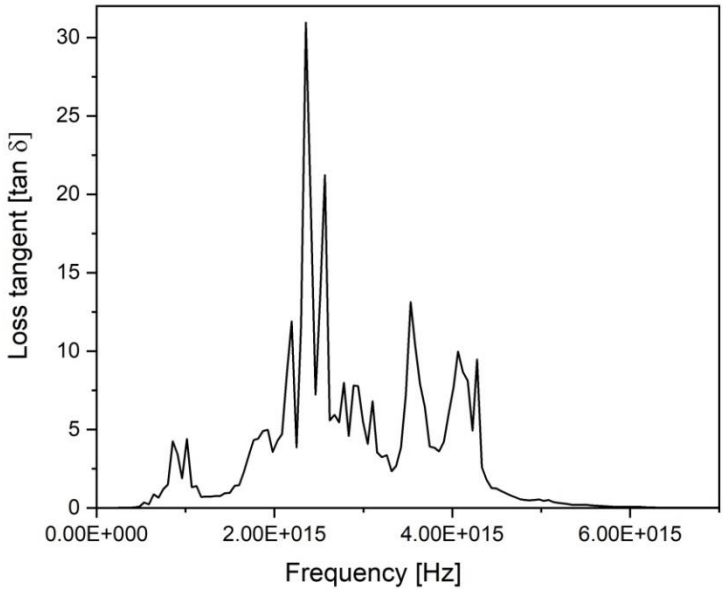

Figure 5. 10 Loss Tangent of cubic $CH_3NH_3SnI_3$

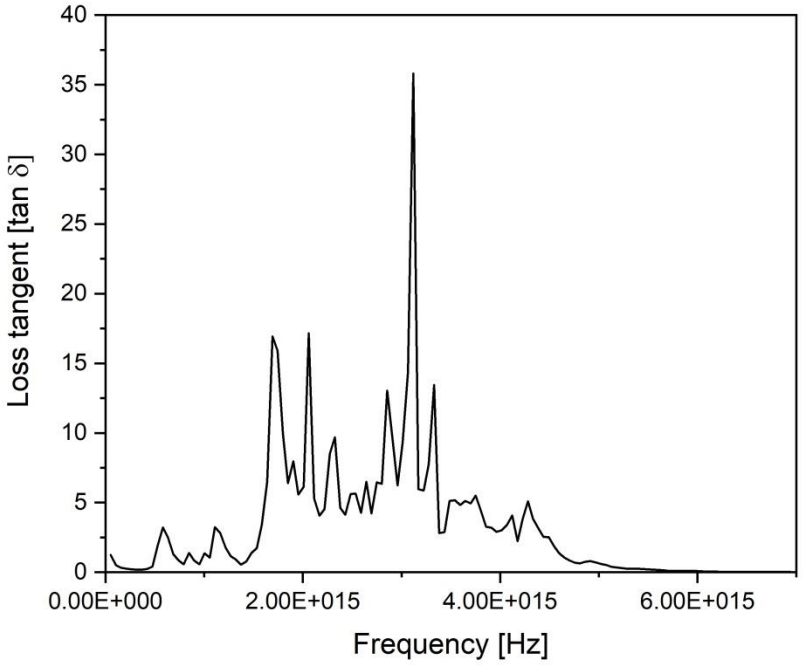

Figure 5. 11 Loss Tangent of cubic $CH_3NH_3BiI_3$

All the above loss tangent data shows the energy lossiness at frequencies of visible region. Maximum and average loss tangents of above investigated materials are listed below.

Table 5. 4 Comparison of loss tangent

Materials	Maximum	Average
Cubic $CH_3NH_3PbI_3$	30.095	1.696
Cubic $CH_3NH_3SnI_3$	30.956	2.084
Cubic $CH_3NH_3BiI_3$	35.819	2.142

Therefore $CH_3NH_3BiI_3$ exhibit a higher dielectric loss tangent while $CH_3NH_3PbI_3$ shows the lowest. $CH_3NH_3PbI_3$ should have higher energy saving ability compared to other two materials while $CH_3NH_3BiI_3$ shows the lowest capacity.

CHAPTER6 CONCLUSIONS

Analysis of the computational results ensure why tetragonal $CH_3NH_3PbI_3$ perform well as a solar absorbing material compared to cubic $CH_3NH_3SnI_3$ and $_{cubic}$ $CH_3NH_3BiI_3$. The energy band gap near to the optimum band gap of 1.34 eV, the higher charge carrier mobility and the higher absorption coefficient are key factors, identified in this study which make $CH_3NH_3PbI_3$ an efficient material. Both $CH_3NH_3SnI_3$ and $CH_3NH_3BiI_3$ show comparable band gap and effective masses. In terms of Dielectric properties $CH_3NH_3PbI_3$ shows higher energy storage capacity than $CH_3NH_3SnI_3$ and $CH_3NH_3BiI_3$. And $CH_3NH_3BiI_3$ has the lowest energy saving ability. However, appropriate band gap engineering technique should be studied to enhance the photovoltaic properties of $CH_3NH_3SnI_3$ and $CH_3NH_3BiI_3$.

CHAPTER7 SUGGESTIONS FOR FUTURE WORK

1. Same calculations should be done with higher accuracy with better computational performance.
2. Computational procedures should be studied to do bivalent cation replacement with more stoichiometric variations (E.g..: $CH_3NH_3Pb_XBi_{1-X}I_3$, etc.).
3. Identified materials should be synthesized and should do relevant testing to find band gap and dielectric function to compare the results of both computational and experiment works.

REFERENCES

[1] G. Kresse, D. Joubert, Kresse, Joubert - Unknown - From ultrasoft pseudopotentials to the projector augmented-wave method, 59 (1999) 11–19.

[2] A.D. Jodlowski, D. Rodríguez-padrón, R. Luque, G. De Miguel, Alternative Perovskites for Photovoltaics, (2018). doi:10.1002/aenm.201703120.

[3] F. Opoku, K.K. Govender, C. Gertina, C. Elizabeth, P.P. Govender, Recent Progress in the Development of Semiconductor- Based Photocatalyst Materials for Applications in Photocatalytic Water Splitting and Degradation of Pollutants, 1700006 (2017) 1–24. doi:10.1002/adsu.201700006.

[4] Z. Wang, B. Lei, X. Xia, Z. Huang, K.P. Homewood, Y. Gao, CH3NH2BiI3 Perovskites: A New Route to Efficient Lead-Free Solar Cells, J. Phys. Chem. C. 122 (2018) 2589–2595. doi:10.1021/acs.jpcc.7b11849.

[5] J. Navas, A. Sánchez-Coronilla, J.J. Gallardo, N. Cruz Hernández, J.C. Piñero, R. Alcántara, C. Fernández-Lorenzo, D.M. De los Santos, T. Aguilar, J. Martín-Calleja, New insights into organic–inorganic hybrid perovskite $CH_3NH_3PbI_3$ nanoparticles. An experimental and theoretical study of doping in Pb^{2+} sites with Sn^{2+}, Sr^{2+}, Cd^{2+} and, Nanoscale. 7 (2015) 6216–6229. doi:10.1039/C5NR00041F.

[6] V. Rao, Computational Study of Structural and Electrical Properties of Methylammonium Lead Iodide Perovskite, 3 (2015) 54–67.

[7] P.S. Whitfield, N. Herron, W.E. Guise, K. Page, Y.Q. Cheng, I. Milas, M.K. Crawford, Structures, Phase Transitions and Tricritical Behavior of the Hybrid Perovskite Methyl Ammonium Lead Iodide, Sci. Rep. 6 (2016) 1–15. doi:10.1038/srep35685.

[8] S. Meloni, G. Palermo, N.A. Astani, B.F.E. Curchod, M. Graetzel, U. Roethlisberger, Valence and conduction bands engineering in halide perovskites for solar cell applica- tions, (2014). http://arxiv.org/abs/1412.3659.

[9] Hilal Ahmad Reshi and Rayees Ahmad Zargar, Perovskite Solar Cells: The Challenging Issues for Stable Power Conversion Efficiency Stable Power Conversion Efficiency, Long-Haul Travel Motiv. by Int. Tour. to Penang. i (2018) 13.

[10] W. Li, Z. Wang, F. Deschler, S. Gao, R.H. Friend, A.K. Cheetham, Chemically diverse and multifunctional hybrid organic-inorganic perovskites, Nat. Rev. Mater. 2 (2017). doi:10.1038/natrevmats.2016.99.

[11] D.W. Kim, I.S. Cho, S.S. Shin, S. Lee, T.H. Noh, D.H. Kim, H.S. Jung, K.S. Hong, Electronic band structures and photovoltaic properties of MWO 4 (M=Zn, Mg, Ca, Sr) compounds, J. Solid State Chem. 184 (2011) 2103–2107. doi:10.1016/j.jssc.2011.06.005.

[12] D.J. Slotcavage, H.I. Karunadasa, M.D. Mcgehee, Light-Induced Phase Segregation in Halide- Perovskite Absorbers, (2016) 1–7. doi:10.1021/acsenergylett.6b00495.

[13] D. Bartesaghi, A. Ray, J. Jiang, R.K.M. Bouwer, S. Tao, T.J. Savenije, D. Bartesaghi, A. Ray, J. Jiang, Partially replacing Pb electronic properties in hybrid metal halide perovskites : Structural and Partially replacing Pb 2 + by Mn 2 + in hybrid metal halide perovskites : Structural and electronic properties, 114206 (2018). doi:10.1063/1.5060953.

[14] C. Zhu, X. Niu, Y. Fu, N. Li, C. Hu, Y. Chen, X. He, G. Na, P. Liu, H. Zai, Y. Ge, Y. Lu, X. Ke, Y. Bai, S. Yang, P. Chen, Y. Li, M. Sui, L. Zhang, H. Zhou, Q. Chen, Strain engineering in perovskite solar cells and its impacts on carrier dynamics, Nat. Commun. (2019). doi:10.1038/s41467-019-08507-4.

[15] E.S. Parrott, T. Green, R.L. Milot, M.B. Johnston, H.J. Snaith, L.M. Herz, Interplay of Structural and Optoelectronic Properties in Formamidinium Mixed Tin – Lead Triiodide Perovskites, 1802803 (2018) 1–11. doi:10.1002/adfm.201802803.

[16] M. Grätzel, L. Han, Efficient and stable large-area perovskite solar cells with inorganic charge extraction layers, (2015) 1–11.

[17] Y. Ogomi, A. Morita, S. Tsukamoto, T. Saitho, N. Fujikawa, Q. Shen, T. Toyoda, K. Yoshino, S.S. Pandey, S. Hayase, CH 3 NH 3 Sn, (2014).

[18] N.K. Noel, S.D. Stranks, A. Abate, C. Wehrenfennig, S. Guarnera, A. Haghighirad, A. Sadhanala, G.E. Eperon, S.K. Pathak, M.B. Johnston, A. Petrozza, M. Herz, H.J. Snaith, Environmental Science for photovoltaic applications †, Energy Environ. Sci. 7 (2014) 3061–3068. doi:10.1039/C4EE01076K.

[19] A. Babayigit, A. Ethirajan, M. Muller, B. Conings, Toxicity of organometal halide perovskite solar cells, Nat. Publ. Gr. 15 (2016) 247–251. doi:10.1038/nmat4572.

[20] M. Abd Mutalib, N. Ahmad Ludin, N.A.A. Nik Ruzalman, V. Barrioz, S. Sepeai, M.A. Mat Teridi, M.S. Su'ait, M.A. Ibrahim, K. Sopian, Progress towards highly stable and lead-free perovskite solar cells, Mater. Renew. Sustain. Energy. 7 (2018). doi:10.1007/s40243-018-0113-0.

[21] D.A. Links, conductivity †, (2011) 5563–5568. doi:10.1039/c0dt01601b.

[22] F.Ã. Meillaud, A. Shah, C. Droz, C. Miazza, Efficiency limits for single-junction and tandem solar cells, (2006) 2952–2959.

[23] C.C. Stoumpos, C.D. Malliakas, M.G. Kanatzidis, Semiconducting tin and lead iodide perovskites with organic cations: Phase transitions, high mobilities, and near-infrared photoluminescent properties, Inorg. Chem. 52 (2013) 9019–9038. doi:10.1021/ic401215x.

[24] F. Hao, C.C. Stoumpos, R.P.H. Chang, M.G. Kanatzidis, Anomalous Band Gap Behavior in Mixed Sn and Pb Perovskites Enables Broadening of Absorption Spectrum in Solar Cells, (2014).

[25] T. Krishnamoorthy, H. Ding, C. Yan, W.L. Leong, T. Baikie, Z. Zhang, M. Sherburne, S. Li, M. Asta, N. Mathews, S.G. Mhaisalkar, Lead-free germanium iodide perovskite materials for photovoltaic applications, J. Mater. Chem. A. 3 (2015) 23829–23832. doi:10.1039/c5ta05741h.

[26] Quantum mechanics and electronic properties of nanostructures, (2005).

[27] J. Hafner, FOUNDATIONS OF DENSITY-FUNCTIONAL THEORY, (n.d.) 1–27.

[28] J. Zaffran, Density Functional Theory applied to the solid state … An introduction to VASP, (n.d.).

[29] S. Lardhi, D. Noureldine, M. Harb, A. Ziani, L. Cavallo, K. Takanabe, S. Lardhi, D. Noureldine, M. Harb, A. Ziani, L. Cavallo, Determination of the electronic , dielectric , and optical properties of sillenite Bi12TiO20 and perovskite-like Bi4Ti3O12 materials from hybrid first-principle calculations Determination of the electronic , dielectric , and optical properties of sillenite Bi 12 TiO 20 and perovskite-like Bi 4 Ti 3 O 12 materials from hybrid first-principle calculations, 134702 (2016). doi:10.1063/1.4945344.

[30] C. Quarti, E. Mosconi, J.M. Ball, V. D'Innocenzo, C. Tao, S. Pathak, H.J. Snaith, A. Petrozza, F. De Angelis, Structural and optical properties of methylammonium lead iodide across the tetragonal to cubic phase transition: Implications for perovskite solar cells, Energy Environ. Sci. 9 (2016) 155–163. doi:10.1039/c5ee02925b.

[31] Z. Shi, A.H. Jayatissa, Perovskites-based solar cells: A review of recent progress, materials and processing methods, Materials (Basel). 11 (2018). doi:10.3390/ma11050729.

[32] W. Ning, F. Gao, Structural and Functional Diversity in Lead-Free Halide Perovskite Materials, Adv. Mater. 31 (2019) 1–21. doi:10.1002/adma.201900326.

[33] F. Sani, S. Shafie, H.N. Lim, A.O. Musa, Advancement on lead-free organic-inorganic halide perovskite solar cells: A review, Materials (Basel). 11 (2018) 1–17. doi:10.3390/ma11061008.

[34] N. Ashari-Astani, S. Meloni, A.H. Salavati, G. Palermo, M. Grätzel, U. Rothlisberger, Computational characterization of the dependence of halide perovskite effective masses on chemical composition and structure, J. Phys. Chem. C. 121 (2017) 1–29. doi:10.1021/acs.jpcc.7b04898.

[35] Y.Q. Huang, J. Su, Q.F. Li, D. Wang, L.H. Xu, Y. Bai, J. Su, Q.F. Li, D. Wang, L.H. Xu, Y. Bai, Structure, optical and electrical properties of CH3NH3SnI3 single crystal, (2019). doi:10.1016/j.physb.2019.03.035.

[36] A.L. Abdelhady, M.I. Saidaminov, B. Murali, V. Adinolfi, O. Voznyy, K. Katsiev, E. Alarousu, R. Comin, I. Dursun, L. Sinatra, E.H. Sargent, O.F. Mohammed, O.M. Bakr, Heterovalent Dopant Incorporation for Bandgap and Type Engineering of Perovskite Crystals, J. Phys. Chem. Lett. 7 (2016) 295–301. doi:10.1021/acs.jpclett.5b02681.

[37] R.A. Jishi, O.B. Ta, A.A. Sharif, Modeling of lead halide perovskites for photovoltaic applications, J. Phys. Chem. C. 118 (2014) 28344–28349. doi:10.1021/jp5050145.

[38] Q. Jiang, T. Xu, Organic-Inorganic Hybrid Perovskite Materials for "Nova Star" Solar Cells: State of Technology and Outstanding Challenges, Comments Inorg. Chem. 36 (2016) 200–214. doi:10.1080/02603594.2015.1116985.

[39] F. Fouladi, Y. Seyed, F. Kanjouri, Results in Physics MAPbI 3 and FAPbI 3 perovskites as solar cells : Case study on structural , electrical and optical properties, Results Phys. 10 (2018) 616–627. doi:10.1016/j.rinp.2018.07.007.

[40] E.S. Parrott, R.L. Milot, T. Stergiopoulos, H.J. Snaith, M.B. Johnston, L.M. Herz, Effect of Structural Phase Transition on Charge-Carrier Lifetimes and Defects in CH3NH3SnI3 Perovskite, J. Phys. Chem. Lett. 7 (2016) 1321–1326. doi:10.1021/acs.jpclett.6b00322.

[41] C. Soykan, H. Gocmez, The physical properties of bismuth replacement in lead halogen perovskite solar cells: CH3NH3Pb1-Bi I3 compounds by ab-initio calculations, Results Phys. (2019) 102278. doi:10.1016/j.rinp.2019.102278.

[42] T. Wang, B. Daiber, J.M. Frost, S.A. Mann, E.C. Garnett, A. Walsh, B. Ehrler, Indirect to direct bandgap transition in methylammonium lead halide perovskite, Energy Environ. Sci. 10 (2017) 509–515. doi:10.1039/c6ee03474h.

[43] T. Kirchartz, U. Rau, Linking structural properties with functionality in solar cell materials-the effective mass and effective density of states, Sustain. Energy Fuels. 2 (2018) 1550–1560. doi:10.1039/c7se00622e.

[44] M.H. Eisa, Results in Physics Electronic structure and optical properties of Cd co-doped wurtizte GaN exposed from fi rst principles study, Results Phys. 13 (2019) 102330. doi:10.1016/j.rinp.2019.102330.

[45] C. Motta, F. El-mellouhi, S. Sanvito, Charge carrier mobility in hybrid halide perovskites, Nat. Publ. Gr. (2015) 1–8. doi:10.1038/srep12746.

[46] L.M. Herz, Charge-Carrier Mobilities in Metal Halide Perovskites: Fundamental Mechanisms and Limits, (2017). doi:10.1021/acsenergylett.7b00276.

[47] W. Wunderlich, H. Ohta, K. Koumoto, Enhanced effective mass in doped SrTiO3 and related perovskites, Phys. B Condens. Matter. 404 (2009) 2202–2212. doi:10.1016/j.physb.2009.04.012.